Frontiers in Bioscience Landmark

Front. Biosci. (Landmark Ed) **2026**; 31(8): 54998
https://doi.org/10.31083/FBL54998

Original Research

Matrix Protective and Anti-Inflammatory *In Vitro* Potential of Adipose Mesenchymal Stromal Cell-Derived EVs Coupled With Platelet-Derived Fibrin Gel

Enrico Ragni[1,*], Michela Taiana[1], Simona Landoni[1], Federico Valli[2], Andrea Massimiliano Nebuloni[1], Paola De Luca[1], Lorenza Lazzari[3], Laura de Girolamo[1], Giuseppe Peretti[4,5]

[1]Laboratorio di Biotecnologie Applicate all'Ortopedia, IRCCS Ospedale Galeazzi-Sant'Ambrogio, 20157 Milan, Italy
[2]Department of Chirurgia Articolare Sostitutiva e Chirurgia Ortopedica, IRCCS Ospedale Galeazzi-Sant'Ambrogio, 20157 Milan, Italy
[3]Unit of Cell and Gene Therapies, Fondazione IRCCS Ca' Granda Ospedale Maggiore Policlinico, 20122 Milan, Italy
[4]Department of Biomedical Sciences for Health, University of Milan, 20133 Milan, Italy
[5]Équipe Universitaria di Ortopedia Rigenerativa e Ricostruttiva, IRCCS Ospedale Galeazzi-Sant'Ambrogio, 20157 Milan, Italy
*Correspondence: enrico.ragni@grupposandonato.it (Enrico Ragni)
Academic Editor: Nikos Karamanos
Submitted: 17 June 2026 Revised: 15 July 2026 Accepted: 21 July 2026 Published: 14 August 2026

Abstract

Background: The limited intrinsic repair capacity of articular cartilage impairs tissue regeneration in osteoarthritis (OA). Platelet-rich plasma (PRP) fibrin gels offer a viable autologous scaffold for cartilage repair but often promote fibrous tissue rather than native hyaline structures. Mesenchymal stromal cell-derived extracellular vesicles (MSC-EVs) can overcome this limitation by actively promoting hyaline cartilage formation and suppressing matrix degradation. This study describes and validates a protocol for embedding adipose-derived MSC (ASC)-EVs into PRP gels (PRP-EVs) and evaluates the protective efficacy in human pathologic chondrocytes and synoviocytes. **Methods:** ASC-EVs were isolated via ultracentrifugation, characterized and their microRNA cargo profiled (quantitative reverse-transcription polymerase chain reaction, qRT-PCR). EVs (10×10^9 particles/mL) were loaded into PRP activated with $CaCl_2$ to form a fibrin hydrogel. EV incorporation efficiency, 4-week release kinetics, cellular uptake (two-dimensional [2D] and three-dimensional [3D] microfluidic models) and penetration into OA cartilage explants using coherent anti-Stokes Raman scattering/two-photon excited fluorescence CARS/TPEF microscopy were assessed. To evaluate the biological effects of the PRP-EV gel secretome, we analyzed gene expression (qRT-PCR), collagen I/II/X deposition (immunofluorescence), metalloproteinase activity and nitric oxide release (ELISA) in interleukin-1β-stimulated 3D chondrocyte pellets, alongside gene expression in OA patient-derived synoviocytes (qRT-PCR). **Results:** The protocol demonstrated high EV encapsulation efficiency (60% ± 8 of the input) in PRP gels and steady kinetics yielding a 20% cumulative release over 4 weeks. Released EVs maintained functional integrity, showing matching 2D/3D uptake in target cells and penetrating to depths exceeding 200 µm within 48 hoursinto OA patients' cartilage explants. In 3D chondrocyte pellets, PRP-EVs significantly downregulated catabolic genes (*MMP1*, *MMP3*, *MMP13*), reducing cumulative matrix metalloproteinase (MMP) enzymatic activity, and blunted nitric oxide production and *CCL5* expression. PRP-EVs counteracted PRP-induced fibrosis, significantly increasing the collagen II/I ratio and suppressing hypertrophic collagen X deposition. In synoviocytes, PRP-EVs significantly downregulated key inflammatory, chemotactic, and pain-signaling genes (*CCL2*, *CXCL8*, *CXCL10*, *IL-6*, *COX2*, *NGF*). **Conclusions:** This study demonstrates that embedding ASC-EVs within a PRP fibrin hydrogel creates a bioactive delivery system. *In vitro*, the secretome released from this composite material successfully counteracts pathological processes in osteoarthritis patient-derived chondrocytes and synoviocytes, reducing matrix degradation and inflammation while promoting a hyaline-like cartilage phenotype.

Keywords: mesenchymal stromal cells; extracellular vesicles; platelet rich plasma; platelet gel; cartilage; chondrocytes; synoviocytes; inflammation

1. Introduction

Articular cartilage is a highly specialized, avascular and aneural tissue with a severely limited intrinsic capacity for self-repair [1]. Consequently, focal cartilage lesions, whether resulting from acute trauma or chronic mechanical stress, frequently trigger a progressive cascade of tissue degradation, including synovial inflammation [2], invariably culminating in the onset of early osteoarthritis (OA) [3]. OA represents a leading cause of global disability, characterized by chronic pain, joint stiffness and a profound impairment in quality of life [4]. Current clinical interventions for cartilage defects have yielded varied results, with the existing body of high-level evidence still limited [5]. Therefore, there is an urgent clinical need for innovative therapeutic strategies capable of halting the osteoarthritic cascade and promoting functional, long-term cartilage regeneration.

Over the past decade, mesenchymal stromal cell (MSC)-based therapies have emerged as a promising frontier in musculoskeletal regenerative medicine. MSCs' therapeutic efficacy is predominantly mediated via paracrine signaling [6], including the secretion of extracellular vesicles (EVs) [7]. Adipose-derived MSCs (ASCs) represent a particularly attractive cell source for musculoskeletal diseases due to their abundant availability, ease of isolation from surgical waste tissue and robust immunomodulatory profile [8]. ASC-derived EVs (ASC-EVs) serve as nano-sized shuttles packed with bioactive cargo, and extensive molecular profiling has revealed that the ASC-EVs are highly enriched with protective miRNAs that collectively exert a potent anti-catabolic and anti-inflammatory activity on diseased chondrocytes, synoviocytes and macrophages [9,10,11], effectively shifting the joint microenvironment toward homeostasis. Consistently, ASC-EVs showed promising anti-inflammatory and chondroprotective effects in OA animal models [12,13], with the ability to enhance hyaline cartilage regeneration [14] and Collagen II deposition [15].

Despite their therapeutic potential, the clinical translation of free EV suspensions is severely hindered by major delivery challenges. Intra-articular injections of liquid EV formulations suffer from rapid clearance via synovial fluid drainage and mechanical wash-out during joint motion, preventing the cargo from achieving sustained therapeutic concentrations at the lesion site [16]. To overcome this limitation, biomaterial-based scaffolding has been proposed to localize and prolong EV retention [17]. With respect to non-functionalized structural scaffolds (hydrogels or polymer-based), platelet-rich plasma (PRP)-derived fibrin gels represent a clinically attractive vehicle due to their completely autologous nature, biocompatibility and inherent richness in growth factors [18,19]. However, in cartilage repair, while PRP can effectively stimulate tissue growth, its application at the lesion site often promotes the formation of fibrous tissue rather than native hyaline structures in both animals [20] and humans [21].

To address these limitations, our group recently developed a high-efficiency protocol to embed ASC-EVs in PRP-gels [22], with the aim of combining the proliferative ability of PRP factors and the hyaline-stimulation of ASC-EVs. Notably, in a comparative study, this formulation resulted more effective than the combination of ASCs and PRP-gels in preserving chondrocyte viability and reducing the inflammatory response [23]. The aim of this study was to confirm the robustness of the ASC-EVs incorporation protocol into PRP-gels, and to evaluate the protective features of the combined product in a three-dimensional (3D) model of OA chondrocytes, at both inflammatory and matrix quality levels, with a supplementary focus on pathologic synoviocytes. Our findings will thus establish a robust, clinically scalable pre-clinical framework for the targeted treatment of articular cartilage degeneration.

2. Materials and Methods

2.1 Adipose Tissue Collection, ASC Isolation and Expansion

Waste adipose tissue was obtained from the abdomen of 5 donors (mean 43 years old ± 15; 3 females and 2 males) undergoing aesthetic procedures. All samples were collected at IRCCS Ospedale Galeazzi - Sant'Ambrogio (Équipe Universitaria di Ortopedia Rigenerativa e Ricostruttiva and Re.Ga.In. Departments) between October 2024 and November 2025 (prospective study "Gel di fibrina caricato con vescicole extracellulari per il trattamento delle lesioni cartilaginee delle articolazioni", approved by Comitato Etico Territoriale Lombardia 1 on date 22/05/2024, registered under number CET 186-2024). As previously described [22], the adipose tissue was digested with GMP-grade type I collagenase (Collagenase NB 6 GMP Grade - For Stem Cell Isolation; Nordmark Pharma GmbH, Uetersen, Germany) at 37 °C for 30 min. The resulting digest was filtered through a 100-µm cell strainer and centrifuged for 5 min at 1000 ×g at RT. The released cells were suspended in GMP-manufactured alphaMEM (10-022-CV; Corning, New York, NY, USA) supplemented with GMP-grade 10% FBS (Australia origin, gamma irradiated; Thermo Fisher Scientific, Waltham, MA, USA) and seeded at a density of 5×10^3 cells/cm^2 at 37 °C (5 % CO_2, 95% humidity). Adipose-derived mesenchymal stromal cells (ASCs) were selected based on plastic adherence and utilized at passage 1 or 2 for subsequent analyses. All generated cells were tested and confirmed to be free of mycoplasma contamination (AssayGenie, Dublin, Ireland). All media and reagents were GMP-compliant, including trypsin (CTS™ TrypLE™ Select Enzyme, Thermo Fisher Scientific), PBS (CTS™ DPBS, Thermo Fisher Scientific) and freezing solution (CTS™ Synth-a-Freeze™ Medium, Thermo Fisher Scientific).

2.2 Cartilage Collection, Chondrocyte Isolation and Expansion

Waste articular cartilage was harvested from 5 osteoarthritis patients (Kellgren-Lawrence grade III–IV; mean age 67 years ± 9; 1 female and 4 males) undergoing arthroplasty. All samples were collected at IRCCS Ospedale Galeazzi - Sant'Ambrogio (Équipe Universitaria di Ortopedia Rigenerativa e Ricostruttiva and Re.Ga.In. Departments) between October 2024 and November 2025 (prospective study "Gel di fibrina caricato con vescicole extracellulari per il trattamento delle lesioni cartilaginee delle articolazioni", approved by Comitato Etico Territoriale Lombardia 1 on 22/05/2024, registered under number CET 186-2024). As previously described [22], cartilage samples were digested with 0.15% w/v type II collagenase (Worthington Biochemical Co.) at 37 °C for 22 h. After digestion, samples were filtered through a cell strainer (100 µm) and centrifuged at 376 ×g for 5 min. Chondrocytes were selected by plastic adherence, cultured in Chondrocyte

medium (ScienCell Research Laboratories, Carlsbad, CA, United States) at 37 °C (5 % CO_2, 95% humidity) and used at passage 1. The maintenance of the OA phenotype was induced in chondrocytes by supplementation with 1 ng/mL Interleukin-1β. All generated cell lines were tested and confirmed to be free of mycoplasma contamination (AssayGenie).

2.3 Synovial Membrane Collection, Synoviocyte Isolation and Expansion

Waste synovial membrane was harvested from 4 osteoarthritis patients (Kellgren-Lawrence grade III–IV; mean age 66 years ± 9; 2 females and 2 males) undergoing arthroplasty. All samples were collected at IRCCS Ospedale Galeazzi - Sant'Ambrogio (Équipe Universitaria di Ortopedia Rigenerativa e Ricostruttiva and Re.Ga.In. Departments) between October 2024 and November 2025 (prospective study "Gel di fibrina caricato con vescicole extracellulari per il trattamento delle lesioni cartilaginee delle articolazioni", approved by Comitato Etico Territoriale Lombardia 1 on 22/05/2024, registered under number CET 186-2024). Synovial membranes were minced into small pieces and enzymatically digested at 37 °C for 3 h with 0.25% w/v type I collagenase (Worthington Biochemical Co.). After digestion, samples were filtered through a cell strainer (100 µm) and centrifuged at 376 ×g for 5 min. Synoviocytes were selected by plastic adherence, cultured in Synoviocyte medium (ScienCell Research Laboratories) at 37 °C (5 % CO_2, 95% humidity) and used at passage 1. The maintenance of the OA phenotype was induced in synoviocytes by supplementation with 1 ng/mL Interleukin-1β. All generated cell lines were tested and confirmed to be free of mycoplasma contamination (AssayGenie).

2.4 PRP Collection

PRP was obtained using the clinical-grade Endoret® system (Lot number: BF03108.A; BTI, Vitoria, Álava, Spain), following the manufacturer's instructions, from patients (mean age 55 years ± 1 year; 6 females and 16 males) undergoing regenerative orthopedic procedures. Briefly, whole blood was collected into vacuum tubes containing an anticoagulant additive and immediately inverted 4 to 6 times to ensure stabilization. The tubes were centrifuged horizontally at room temperature within 1 hour of collection using a pre-programmed centrifuge to achieve reproducible separation. Finally, the complete volume of the upper growth factor-rich plasma fraction was recovered via vacuum-assisted aspiration with a Plasma Transfer Device in the kit, while carefully avoiding any contact with the leukocyte buffy coat and the erythrocyte layers to ensure a leukocyte-free formulation. All samples were collected at IRCCS Ospedale Galeazzi - Sant'Ambrogio (Équipe Universitaria di Ortopedia Rigenerativa e Ricostruttiva and Re.Ga.In. Departments) between October 2024 and November 2025 (prospective study "Gel di fibrina caricato con vescicole extracellulari per il trattamento delle lesioni cartilaginee delle articolazioni", approved by Comitato Etico Territoriale Lombardia 1 on 22/05/2024, registered under number CET 186-2024). Complete blood and PRP cell counts were performed using a Sysmex XN-2000 hematocytometer (Sysmex, Kobe, Japan).

2.5 Flow Cytometry Characterization of Chondrocytes, Synoviocytes and ASCs

Staining of cells was performed at 4 °C for 30 min in the dark with the fluorochrome-conjugated antibodies: (i) chondrocytes, anti-CD73-phycoerythrin (PE) (REA804, Miltenyi Biotec, Bergisch Gladbach, Germany; 1:50 dilution), CD44-PE (130-110-293, Miltenyi Biotec; 1:10 dilution) and CD45-PE-Vio770 (REA747, Miltenyi Biotec; 1:50 dilution); (ii) synoviocytes, anti-CD45-fluorescein isothiocyanate (FITC) (REA747, Miltenyi Biotec; 1:50 dilution), CD14-PC5 (301863, Biolegend, San Diego, CA, USA; 1:20 dilution) and CD73-allophycocyanin (APC)-A700 (344041, Biolegend, 1:20); anti- (iii) ASCs, anti-CD90-FITC (REA897, Miltenyi Biotec; 1:50 dilution), CD73-PE (REA804, Miltenyi Biotec; 1:50 dilution), CD105-PerCP-Cy5.5 (43A3, BioLegend; 1:20 dilution) and CD45-PE-Vio770 (REA747, Miltenyi Biotec; 1:50 dilution). After a washing step, at least 30,000 events per sample were tested with a CytoFLEX flow cytometer (Beckman Coulter, Fullerton, CA, USA).

2.6 ASC Secretome Production and EVs Isolation

Upon reaching 90% confluence, ASCs were washed three times with GMP-grade PBS and 12 mL of FBS-free GMP-grade alphaMEM was added to each T175 flask. After 48 h of incubation, the conditioned medium (secretome) was collected and subjected to serial centrifugations at 376 ×g, 1000 ×g, 2000 ×g and twice at 4000 ×g (each run at 4 °C for 15 min) to get rid of debris and dead cells. For EVs isolation, cell culture supernatants were centrifuged at 4 °C for 3 h at 100,000 ×g using a 70Ti fixed-angle rotor (Beckman Coulter). The resulting EV-containing pellets were washed with GMP-grade PBS and suspended in GMP-grade PBS. After quantification with a NanoSight NS300 system (capturing five 60 s videos) (NanoSight Ltd., Amesbury, UK), the particle amount was determined using NTA software v3.4 (NanoSight Ltd.) and EV final concentration was set to 10×10^{10} particles/mL with GMP-grade PBS. Aliquots containing 10×10^9 EVs were then stored at –80 °C. Starting ASCs were detached, counted and evaluated for viability using a NucleoCounter NC-3000 (ChemoMetec, Allerod, Denmark).

2.7 Characterization of EVs

Flow Cytometry: EVs were stained with the MACSPlex EV Kit IO human (Miltenyi Biotec) according to the manufacturer's protocol. Marker analysis was performed using a CytoFLEX flow cytometer (Beckman Coulter).

Nanoparticle Tracking Analysis (NTA): EVs were analyzed using the NanoSight NS300 system (capturing five 60 s videos) (NanoSight Ltd.), after dilution with PBS to have reads between 20 and 120 particles per frame. Particle concentration and size distribution profiles were determined using NTA software v3.4 (NanoSight Ltd.).

Transmission electron microscopy (TEM): EVs were suspended in PBS and a 5 µL droplet was deposited onto formvar/carbon-coated grids for 10 min at room temperature. Excess liquid was blotted away with filter paper. Negative staining was performed by applying a 2% aqueous uranyl acetate solution for 10 min, and the excess was removed using filter paper. Grids were air-dried at room temperature and subsequently examined using a TALOS L120C transmission electron microscope (Thermo Fisher Scientific) operated at 120 kV.

Purity: EVs were analyzed with a NanoDrop ND-1000 spectrophotometer (Thermo Fisher Scientific) with the Protein A280 protocol. The concentration was related to NTA data to obtain the number of EVs/µg protein value.

2.8 Quantification of EV-derived miRNAs

EVs pooled into a single batch were disrupted in TRIzol reagent, and total RNA was extracted using the miRNeasy and RNeasy CleanUp kits (Qiagen, Hilden, Germany) following the manufacturer's instructions. Briefly, samples were homogenized, incubated at room temperature and mixed with chloroform before being shaken vigorously and allowed to settle. Phase separation was achieved by centrifugation, after which the upper aqueous phase was carefully transferred to a new tube and the volume adjusted with RNase-free water. Buffer RLT was added to the solution, mixed thoroughly and then ethanol was added. The resulting mixture was loaded onto a spin column, centrifuged and the flow-through was discarded, with this step repeated for any remaining volume. The column was washed, followed by centrifugation and removal of the flow-through. Ethanol was then applied to the column, which was centrifuged again before discarding the collection tube and placing the column into a new one. To ensure complete drying of the membrane, the column was centrifuged with its cap open. Finally, the spin column was transferred to a new collection tube, and RNA elution was performed by adding RNase-free water directly onto the center of the membrane followed by a final centrifugation step. To monitor technical variability during isolation and subsequent downstream reactions, 6 pg of a synthetic non-human miRNA spike-in (*Arabidopsis thaliana* ath-miR-159a) was added to each sample, allowing for potential normalization of panels A and B on the OpenArray® platform (Thermo Fisher Scientific). Standard reverse transcription and pre-amplification protocols were performed using independent A and B kits to generate the corresponding cDNAs. Real-time RT-PCR analysis was executed using the QuantStudio™ 12K Flex OpenArray® platform (QS12KFlex). Expression data for EV-derived miRNAs from panels A and B, which collectively cover 754 well-characterized human miRNA sequences according to the miRBase database v21 (Sanger), were processed using the Gene Expression Suite Software v1.3 (Thermo Fisher Scientific). The first quartile of Ct values was determined. The percentage of the genetic message contributed by each individual miRNA was calculated using the following workflow: calculation of the ΔCt values between the most abundant miRNA and all other targets; calculation of the $2^{-\Delta Ct}$ value for each miRNA; summation of the $2^{-\Delta Ct}$ values; calculation of the individual percentage for each miRNA using the formula: ($2^{-\Delta Ct}$ of a given miRNA / summation of the $2^{-\Delta Ct}$ of all miRNAs) × 100. Network and Function analyses were performed with the miRNet platform (https://www.mirnet.ca/miRNet/home.xhtml) under default settings and miRTarBase V9.0 targets [24].

2.9 Preparation of Fluorescent EVs

Pooled secretomes were incubated with 10 µM of 5(6)-carboxyfluorescein diacetate succinimidyl ester (CFDA-SE, Sigma-Aldrich, St. Louis, MO, USA) for 1 h at 37 °C in the dark. Fluorescent EVs were subsequently purified utilizing the ultracentrifugation protocol previously described. The obtained EV pellets were aliquoted into vials at a concentration of 10×10^9 particles and stored at –80 °C until use.

2.10 Platelet Gel Preparation and EV Incorporation

Prior to activation, PRP samples were divided into two 1-mL aliquots and supplemented as follows: either with an ASC-derived EV suspension (10×10^9 EVs per mL of PRP, fluorescent or unstained depending on the assay) or with an equivalent volume of EV-free vehicle control. The PRP samples were then activated by adding final 22.8 mM $CaCl_2$ and incubated for 2 h at 37 °C to induce clot formation. Following gelation, the resulting fibrin clots and the overlying supernatant fluids were collected separately and either used immediately or stored at –80 °C for further analysis.

2.11 Quantification of EV Incorporation Efficiency and Release Kinetics

Platelet gels were carefully separated from the clotting solution and weighed to determine their wet mass. To evaluate release kinetics, a volume of PBS or serum-free medium equivalent to twice the wet mass of the gel in milligrams was added to each vehicle or EV-loaded gel (e.g., 200 µL of buffer for a 100 mg gel). At 24 hours, the supernatant was harvested completely and immediately replaced with an identical volume of fresh buffer. This sampling procedure was systematically repeated at 48 hours, and at 1, 2, 3 and 4 weeks. Collected supernatants were either analyzed immediately by flow cytometry or stored at –80 °C for subsequent analysis.

For quantitative assessment, the collected fractions were analyzed using a CytoFLEX flow cytometer (Beck-

man Coulter, Brea, CA, USA). Analyzed samples included the initial PRP prior to clotting (either with or without CFSE-labeled EVs), the post-gelation supernatants, and the release fractions harvested after incubation with the buffer. Fluorescent nanobeads in the FITC range with diameters of 100, 160, 200, 240, 300, 500 and 900 nm (Biocytex, Marseille, France) were employed as internal size standards. Fluorescent EVs were detected and gated in the FITC channel, utilizing EV-free PRP as a negative background control. A minimum of 30,000 events was acquired for each sample. The absolute number of EV events was calculated using the following conversion formula: Total EV Events = Events/s (FITC) × Acquisition Rate (s/µL) × Dilution Factor × Total Volume (µL). Comparative analysis across samples was performed to determine the percentage of released EVs relative to the baseline input (10×10^9 EVs).

2.12 Uptake of Platelet Gel-Released EVs by OA Chondrocytes in a 2D Model

Passage 1 OA chondrocytes were seeded at a density of 10,000 cells/cm^2. After 24 hours, four experimental conditions were applied: (i) control treatment with IL-1β (1 ng/mL); (ii) purified fluorescent EVs (25,000 particles/cell); (iii) 48-hour supernatant harvested from fluorescent EV-loaded gels; and (iv) 48-hour supernatant harvested from EV-free vehicle gels. The absolute number of EVs in each experimental condition was quantified via flow cytometry (FITC events/volume). All culture conditions were supplemented with 10% ultracentrifuged FBS to ensure depletion of endogenous bovine EVs. After 48 hours of incubation, chondrocytes were harvested and analyzed for FITC fluorescence intensity using a CytoFLEX flow cytometer (Beckman Coulter, Brea, CA, USA), acquiring a minimum of 30,000 events per sample. Data were expressed as mean fluorescence intensity (MFI).

2.13 EVs Uptake by OA Chondrocytes in a Microfluidic Model

Passage 1 OA chondrocytes were cultured within microfluidic chips. Prior to seeding, chondrocytes were labeled with CellTracker™ Deep Red Dye (Thermo Fisher Scientific, Waltham, MA, USA), subsequently suspended in human thrombin (4 UI/mL in 40 mM $CaCl_2$), and mixed at a 1:1 ratio with human fibrinogen (20 mg/mL). This mixture was immediately injected into the designated gel channels of the chip and allowed to polymerize at room temperature for 7 minutes. Fluorescent purified or gel-released EVs (25,000 particles/cell) were then introduced into the central fluidic channel. After 48 hours, the chips were fixed with 2% paraformaldehyde (PFA) and imaged using a Leica SP8 confocal microscope (Leica Microsystems, Wetzlar, Germany), capturing 150 µm z-stacks at 1 µm intervals. Cell-EV interactions and colocalization were quantified using ImageJ software v1.48 (NIH, Bethesda, MD, USA) equipped with a custom macro script.

2.14 EVs Penetration Into OA Cartilage

OA cartilage explants measuring approximately 0.5 × 0.5 cm (thickness 0.5–1 mm) were placed into 12-well plates. A section of platelet gel (either vehicle control or fluorescent EV-loaded) was positioned directly on top of each cartilage piece. Medium was carefully added to submerge the system without causing the gel to float. Following a 48-h incubation period, the tissue samples were harvested and examined via Coherent Anti-Stokes Raman Scattering (CARS) microscopy to visualize the extracellular matrix and two-photon excited fluorescence (TPEF) microscopy to track the fluorescent EVs as previously described [22]. Briefly, for image acquisition, the CARS signal was targeted at the CH_2 stretching mode (2848 cm^{-1}). The optical setup comprised an Nd:YVO_4 laser emitting 10-ps pulses centered at 1064 nm (Picotrain, HighQLaser, Austria) to provide the Stokes field, and the signal output of an Optical Parametric Oscillator (Levante Emerald OPO, APE, Germany), tuned to approximately 817 nm with a pulse width of 6 ps, to serve as the pump field. The laser repetition rate was maintained at 76 MHz. The collinearly aligned beams were directed into an upright microscope (BX51WI, Olympus, Tokyo, Japan) through a laser scanning unit (FluoView FV300, Olympus). The same 817-nm OPO signal output served as the excitation source for TPEF imaging. The total average excitation power at the sample plane was adjusted to approximately 40 mW. Excitation beams were focused onto the living samples using a water immersion objective (LUMPLFLN 40XW, NA = 0.8, W.D. = 3.3 mm, Olympus), which was cleaned and sterilized with a 70% ethanol/water (v/v) solution prior to each experiment. A condenser lens (UPLSAPO 10X, NA = 0.4, Olympus) was positioned to collect the forward CARS signal at approximately 663 nm, which was subsequently optically filtered and detected using a photomultiplier tube (PMT; R3896, Hamamatsu, Japan). Concurrently, the TPEF signal was acquired in a back-scattering (epi-detection) geometry. The depth of EV penetration, alongside the average occupied area and volume, was quantified using a custom-made ImageJ plugin designed to process 3D image stacks.

2.15 Gene Expression Evaluation in OA Chondrocytes

Passage 1 OA chondrocytes were seeded in ultra-low attachment 96-well plates at a concentration of 250,000 cells, in a final volume of 200 µL. After seeding, cells were centrifuged at 300 ×g for 2 minutes to form pellets. After 48 hours, cells were treated with either purified EVs or 48-h gel supernatants (without or with EVs). When present, EVs were administered at a concentration of 25,000 particles/cell. Treatment was performed for 14 days, with medium changes every 2 days. At the end of treatment, for gene expression evaluation, cells were lysed and total RNA was extracted using the miRNeasy Kit (Qiagen) as per paragraph 2.8. The isolated RNA was reverse-transcribed using the iScript cDNA Synthesis Kit

(Bio-Rad, Hercules, CA, USA) and subjected to RT-qPCR analysis using iTaq Universal SYBR Green Supermix (Bio-Rad) on a CFX Opus 96 Real-Time PCR System (Bio-Rad). *RPLP0* (F: TGTGGGCTCCAAGCAGATGCA, R: GCAGCAGTTTCTCCAGAGCTGGG) was utilized as the reference housekeeping gene. Tested genes were: *MMP1* (F: ACAACTGCCAAATGGGCTTG, R: AACAGCCCAGTACTTATTCCCTT), *MMP3* (F: CGTGCTTTGTCCTTTGATGCTG, R: GCGCCAAAAGTGCCTGTCTT), *MMP13* (F: GTGCAGCTGTTCACTTTGAGG; R: ATCATATCTCCAGACCTGGTTTC) and *CCL5* (F: GGTACCATGAAGGTCTCCGC, R: GGTGTCCGAGGAATATGGGG).

2.16 Collagen Deposition Evaluation in OA Chondrocytes

Chondrocytes were treated as per section 2.15. At the end of treatment, the specimens were first rinsed with PBS and then fixed in 10% neutral buffered formalin for 2 hours at room temperature. Following fixation, the samples underwent three sequential washes in PBS for 15 minutes each. For cryoprotection, the specimens were incubated in a 30% sucrose solution in water overnight at 4 °C. The following day, a graded infiltration was performed at room temperature using mixtures of 30% sucrose and Optimal Cutting Temperature (OCT) compound. Specifically, the samples were incubated for 30 minutes in a 2:1 ratio mixture (4 mL of 30 % sucrose and 2 mL of OCT), followed by 30 minutes in a 1:1 ratio mixture (3 mL of 30 % sucrose and 3 mL of OCT), and a final 30-minute incubation in a 1:2 ratio mixture (2 mL of 30 % sucrose and 4 mL of OCT). Finally, the sample pellets were cryosectioned at 8 µm. Cryosections were co-stained with antibodies against Collagen II (ab307674) and Collagen I (ab6308), or Collagen X (ab260040) (all 1:200, Abcam, Cambridge, UK), followed by species-appropriate AlexaFluor 488/594 secondary antibodies (1:1000, Thermo Fisher Scientific) and DAPI mounting medium. Images were acquired sequentially on a Leica TCS-SP8 confocal microscope (60×) (Leica Camera AG, Wetzlar, Germany). Five sections per sample were analyzed; for each section, three to five fields were imaged. The Col II/Col I integrated density ratio was quantified using ImageJ as an index of cartilage matrix integrity, alongside absolute integrated densities of Collagen X.

2.17 Released Matrix Metalloproteinase (MMP) Activity in OA Chondrocytes

Chondrocytes were treated as per section 2.15. At the end of treatment, supernatants over 2 weeks of treatment were collected at each medium change and stored at –20 °C. MMP activity was assessed using the SensoLyte 520 Generic MMP Assay Kit (AnaSpec, Fremont, CA, USA) following the manufacturer's instructions. To trigger pro-MMP activation, samples were incubated with 1 mM 4-aminophenylmercuric acetate (APMA) at 37 °C for 3 hours. Fluorescence intensity (excitation λ = 490 nm, emission λ = 520 nm) was measured using a Wallac Victor II microplate reader (PerkinElmer, Waltham, MA, USA). Background fluorescence (assay buffer) was subtracted from all sample readings. The cumulative MMP activity across the 2 weeks of treatment was finally calculated.

2.18 Released Nitric Oxide (NO) Evaluation in OA Chondrocytes

Chondrocytes were treated as per section 2.15. At the end of treatment, supernatants over 2 weeks of treatment were collected at each medium change and stored at –20 °C. Total nitrite and nitrate levels were measured using the Griess Reagent Kit (ab272517, Abcam). Nitrates were enzymatically reduced to nitrites prior to colorimetric detection via the Griess reaction. Absorbance at 540 nm was measured with a Wallac Victor II microplate reader (PerkinElmer).

2.19 Biological Activity of EV-Loaded Gels on OA Synoviocytes

Passage 1 OA synoviocytes were seeded at a density of 20,000 cells/cm^2. After 24 h, cells were treated with either purified EVs or 48-h PRP gel supernatants (without or with EVs). When present, EVs were administered at a concentration of 25,000 particles/cell. Following a 48-h incubation, cells were lysed and total RNA was extracted using the miRNeasy Kit (Qiagen) as per paragraph 2.8. The isolated RNA was reverse-transcribed using the iScript cDNA Synthesis Kit (Bio-Rad) and subjected to RT-qPCR analysis using iTaq Universal SYBR Green Supermix (Bio-Rad) on a CFX Opus 96 Real-Time PCR System (Bio-Rad). *TBP* (F: GCCACGCCAGCTTCGGAGAG, R: CCGCAGCAAACCGCTTGGGA) was utilized as the reference housekeeping gene. Tested genes were: *CCL2* (F: GCAATCAATGCCCCAGTCAC, R: CTTGAAGATCACAGCCTTCTTTGG), *CCL5* (F: GGTACCATGAAGGTCTCCGC, R: GGTGTCCGAGGAATATGGGG), *CXCL8* (F: ACCGGAAGGAACCATCTCAC, R: GGCAAAACTGCACCTTCACAC), *CXCL9* (F: AGTGCAAGGAACCCCAGTAG, R: AGGGCTTGGGGCAAATTGTT), *CXCL10* (F: AAGTGGCATTCAAGGAGTACC, R: ACGTGGACAAAATTGGCTTGC), *IL6* (F: ATCTGGATTCAATGAGGAGACTTG, R: TTGTACTCATCTGCACAGCTC), *CD44* (F: CTGGCGCAGATCGATTTGAATA, R: TCCGTCCGAGAGATGCTGTA), *HAS1* (F: TGCTACCAAGTACACCTCCAG, R: GTTGTACAGCCACTCACGGA), *HAS2* (F: TTGGGGGAGATGTCCAGATTTTT, R: AATGCACTGAACACACCCAA), *HAS3* (F: GACTACATCCAGGTGTGCGA, R: ATCCTCCTCCAGGACTCGAA), *ICAM1* (F: TTCGTGTCCTGTATGGCCC, R: CACATTGGAGTCTGCTGGGA), *IL10* (F: AAGACCCAGACATCAAGGCG, R: CAGGGAAGAAATCGATGACAGC), *TGF* (F: TCCTGGCGATACCTCAGCAA, R: CTCAATTTCCCCTCCACGGC),

IDO (F: GCTAAAGGCGCTGTTGGAAA, R: TTGCCTTTCCAGCCAGACAAA), *COX2* (F: CAAATTGCTGGCAGGGTTGC, R: AGGGCTTCAGCATAAAGCGT) and *NGF* (F: GGAGCGCAGCGAGTTTTGG, R: AGTGTGGCCAGGATAGAAAGC).

2.20 Hierarchical Clustering and Principal Component Analysis

Hierarchical clustering and principal component analysis were obtained with the ClustVis package v2.0 https://biit.cs.ut.ee/clustvis/ [25]. For chondrocyte gene expression, MMPs activity and NO release analysis through a heatmap with hierarchical clustering was generated: gene expression abundance ratios were calculated from –ΔCt data ($2^{-\Delta Ct}$) and the IL-1β condition was set as 1; MMPs and NO values were input as ratios with respect to the IL-1β condition set as 1. Input values were ln(x+1)-transformed. Unit variance scaling was applied to rows. Both rows and columns were clustered using correlation distance and average linkage. For synoviocytes gene expression analysis: abundance ratios were calculated from –ΔCt data ($2^{-\Delta Ct}$) and the IL-1β condition was set as 1. For PCA, no scaling was applied to rows; SVD with imputation was used to calculate principal components. For the heatmap with hierarchical clustering, no scaling was applied to rows. Both rows and columns were clustered using correlation distance and average linkage.

2.21 Statistical Analysis

Statistical analysis was performed using GraphPad Prism software, v8.0.2 (GraphPad Software, San Diego, CA, USA). To ensure technical reproducibility and confirm that the current two-dimensional (2D) and 3D microfluidic incorporation profiles were equivalent to our previously published baseline protocol [22], separate *a priori* equivalence power analyses were performed during the study design phase. Calculations were based on historical mean and standard deviation benchmarks for both experimental setups of the previous publication. Utilizing a Two One-Sided Tests framework with an equivalence bound (delta) set at ± 20% of the baseline means, the statistical power analysis independently determined that a sample size of n = 3 independent runs per assay was sufficient to achieve a statistical power >80 % at a significance level of alpha = 0.05 to successfully reject the hypothesis of inequivalence. Consequently, an n = 3 sample size was adopted for subsequent microfluidic validation experiments. For the multi-group comparative assays involving four experimental conditions in pathologic chondrocytes and synoviocytes, the sample size was determined through an *a priori* power analysis for a One-Way Analysis of Variance (ANOVA). Assuming a large anticipated therapeutic effect size (Cohen's f = 1.15), the power analysis indicated that a minimum of n = 3 independent biological replicates per group was required to ensure a statistical power >80 % with a significance level of alpha = 0.05. Accordingly, all comparative experiments were executed with a sample size of $n \geq 3$. Data distribution normality was assessed using the Shapiro-Wilk normality test (alpha = 0.01). For comparisons involving more than two conditions, a one-way repeated measures ANOVA was performed, followed by Tukey's post-hoc test for multiple comparisons. In the event of non-normal distributions, the non-parametric Friedman test was employed alongside Dunn's post-hoc test. For fold-change and ratio data analyses, a one-sample *t*-test was conducted, establishing the null hypothesis value at 1. For all statistical tests, the threshold for significance was set at $p \leq 0.05$. Values are expressed as mean ± standard deviation (SD).

3. Results

3.1 Phenotypic Characterization of ASCs and EVs

ASCs were strongly positive for the mesenchymal markers CD73 (100% ± 0) and CD90 (98% ± 1), weakly positive for CD105 (14% ± 6) (n = 5) and negative for the hematopoietic marker CD45 (2% ± 1) (Fig. 1A).

After starvation, cell viability was 92% ± 3. NTA of the EVs revealed a consistent profile across donors, with a mean size of 182 nm ± 26, a mode of 117 nm ± 12 and a D50 of 150 nm ± 23 (Fig. 1B). The particles were fully positive (100%) for the classical EV markers CD63 and CD81, with CD9 expressed at lower levels (42% ± 9) (Fig. 1C). Regarding mesenchymal markers, the EVs exhibited the presence of CD29 (26% ± 4), CD44 (17% ± 4), CD49e (19% ± 4) and CD105 (20% ± 3) (Fig. 1C). Transmission electron microscopy confirmed the presence of EVs in the preparations, displaying their characteristic cup-shaped morphology (Fig. 1D). Finally, EV purity was 5.7×10^9 ± 0.3 EVs/µg protein.

3.2 miRNAs Associated With EVs

Three hundred and sixty-four miRNAs were detected in EVs (**Supplementary Table 1**). Network analysis on the whole dataset identified 11 hub miRNAs with more than 50 interactions, with hsa-miR-16-5p having 132 interactors, hsa-miR-29b-3p 113, hsa-miR-26a-5p 107 and hsa-miR-24-3p 100. A deeper miRNA Function analysis with a focus on joints homeostasis identified players involved in Chondrogenic differentiation (hsa-miR-29a-3p, hsa-miR-29a-5p, hsa-miR-30a-3p, hsa-miR-30a-5p and hsa-miR-140-3p; $p = 0.00188$) and 16 in Immune Response (hsa-miR-15a-3p, hsa-miR-16-5p, hsa-miR-18a-3p, hsa-miR-19b-3p, hsa-miR-29b-3p, hsa-miR-30a-3p, hsa-miR-30a-5p, hsa-miR-92a-3p, hsa-miR-100-3p, hsa-miR-100-5p, hsa-miR-101-3p, hsa-miR-103a-3p, hsa-miR-107, hsa-miR-192a-5p, hsa-miR-500a-5p and hsa-miR-532-5p; $p = 0.0169$). Supporting this notion, 3 transcription factors emerged as regulated, STAT5 which is involved in OA progression (hsa-miR-25a-3p, hsa-miR-17-3p, hsa-miR-17-5p, hsa-miR-18a-3p, hsa-miR-19a-3p and hsa-miR-20a-5p; $p = 0.00243$), AP-1 which is involved in matrix turnover

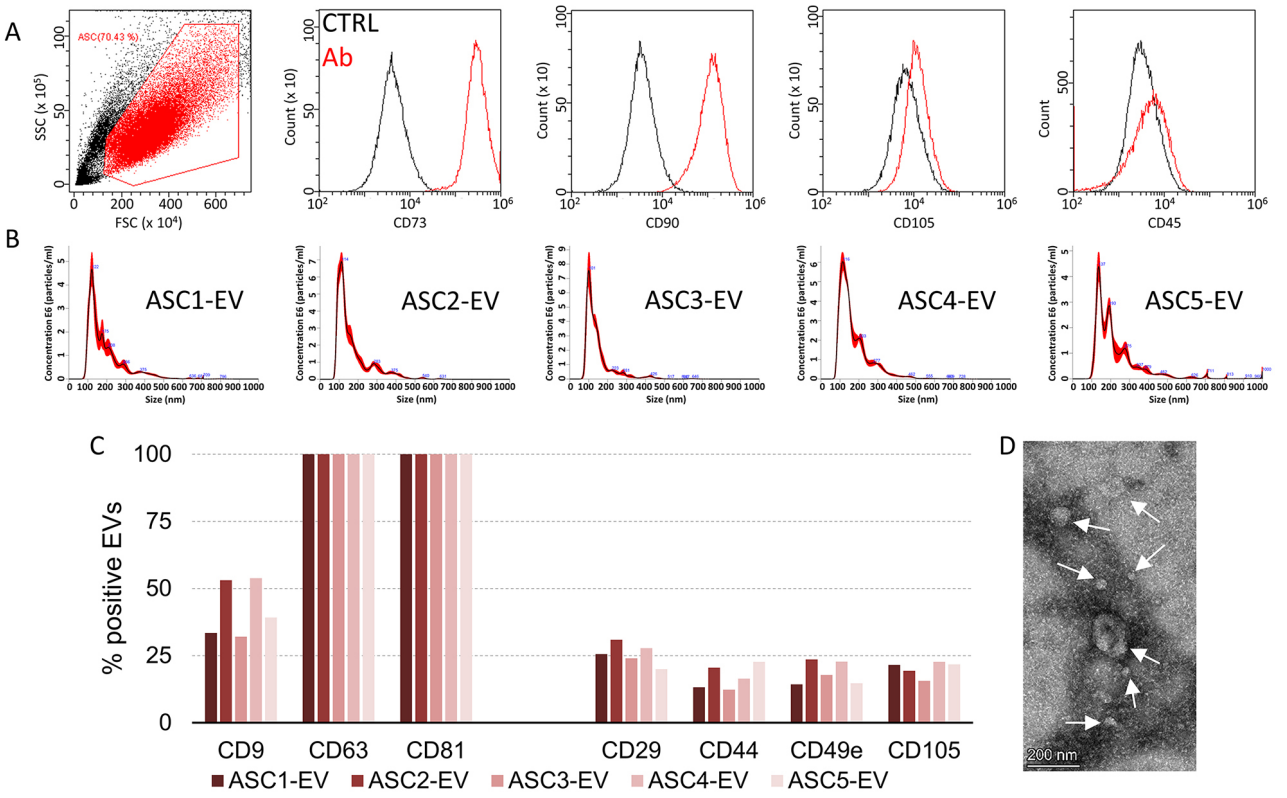

Fig. 1. Phenotype of ASCs and EVs. (A) Immunophenotype of ASCs showing positivity for the lineage markers CD73 and CD90 and negativity for the marker CD45, which is typical of blood cells. Although CD105 is weakly positive, it is present on the entire cell population as demonstrated by the shift of the entire peak relative to the unstained control. The profile of one representative donor is shown. (B) Size distribution profile for the EVs released by the 5 ASCs under analysis. (C) Immunophenotype of EVs. The particles were positive for the typical EV markers CD9, CD63 and CD81, as well as for the ASC markers CD29, CD44, CD49e and CD105. (D) Transmission electron microscopy of EVs. Images from one representative donor are shown, scale bar = 200 nm. White arrows indicate EVs over the background. ASCs, adipose-derived MSCs; EVs, extracellular vesicles.

and MMPs transcription (hsa-miR-21a-5p, hsa-miR-29a-3p, hsa-miR-29a-5p and hsa-miR-29b-3p; $p = 0.00782$) and NFKB1 which the master regulator of inflammatory response in chondrocytes (hsa-miR-let-7a-5p, hsa-miR-16-5p, hsa-miR-17-3p, hsa-miR-17-5p, hsa-miR-21-5p, hsa-miR-29a-3p, hsa-miR-29a-5p, hsa-miR-29b-3p, hsa-miR-199a-3p and hsa-miR-199b-5p; $p = 0.0389$).

To get a sharper picture of EV-miRNAs' function, considering the average presence of a single highly abundant miRNA molecule in EVs from mesenchymal stromal cells, approximately 100 EVs would be required to effectively transfer the genetic message to target cells [26,27]. Therefore, only highly abundant miRNAs accounting for at least 1% of the total identified genetic message were further examined (**Supplementary Table 1**). Table 1 lists the 20 analyzed miRNAs, which together account for 81% of the total genetic message.

To obtain a broader overview of the role of the EV-shuttled miRNAs, their known functions in cartilage homeostasis [28] were analyzed (Table 2). Regarding cartilage, most of the abundant miRNAs possess a protective function. The primary miRNAs involved were found to be miR-24-3p (16.5%), miR-222-3p (4.8%) and miR-193b-3p (4.2%), with a total cumulative weight for this category equal to 27%. This value drops drastically for the 3 identified miRNAs with a destructive function, which account for only 7.2%, representing a nearly 4-fold decrease. Additionally, 3 miRNAs with dual functions were identified, carrying a weight of 18.2%.

3.3 EVs Are Efficiently Incorporated Into Platelet Gels and Are Released Over Time

The amount of EVs incorporated into the platelet gels was 60% ± 8 (n = 6) of those initially added (10×10^9 EVs) to 1 mL of PRP prior to clot formation. Based on the wet weight of the gel, $64 \times 10^6 \pm 27$ EVs were incorporated per mg. EV release was monitored for a period of up to 4 weeks. The quantity and kinetics of EV release per mg of clot are shown in Fig. 2A,B, presenting both time-interval and cumulative data. Within the first 24 hours, 5% ± 2 (n = 6) of the incorporated EVs were released from the clot, followed by an additional 1% ± 0 on day 2. Between days 3 and 7, another 2% ± 4 of the incorporated particles were released. Over the subsequent three weeks, a steady release

Table 1. ASC-EV miRNAs with genetic weight ≥1%.

miRNA	% genetic weight	miRNA	% genetic weight
hsa-miR-24-3p	16.5	hsa-miR-30c-5p	2.5
hsa-miR-125b-5p	11.7	hsa-miR-720	2.4
hsa-miR-520e-3p	8.2	hsa-miR-30b-5p	1.9
hsa-miR-221-3p	4.9	hsa-miR-92a-3p	1.6
hsa-miR-222-3p	4.8	hsa-miR-145-5p	1.5
hsa-miR-618	4.5	hsa-miR-191-5p	1.5
hsa-miR-21-5p	4.3	hsa-miR-99b-5p	1.3
hsa-miR-193b-3p	4.2	hsa-miR-20a-5p	1.1
hsa-miR-100-5p	3.0	hsa-miR-31-5p	1.1
hsa-miR-99a-5p	3.0	hsa-miR-19b-3p	1.0

Table 2. ASC-EV miRNAs (≥1% genetic weight) involved in cartilage homeostasis regulation.

Cartilage					
Protective		Destructive		Double role	
miRNA	% genetic weight	miRNA	% genetic weight	miRNA	% genetic weight
hsa-miR-24-3p	16.5	hsa-miR-21-5p	4.3	hsa-miR-125b-5p	11.7
hsa-miR-222-3p	4.8	hsa-miR-30b-5p	1.9	hsa-miR-221-3p	4.9
hsa-miR-193b-3p	4.2	hsa-miR-19b-3p	1.0	hsa-miR-145-5p	1.5
hsa-miR-92a-3p	1.6				
Total	27.0		7.2		18.2

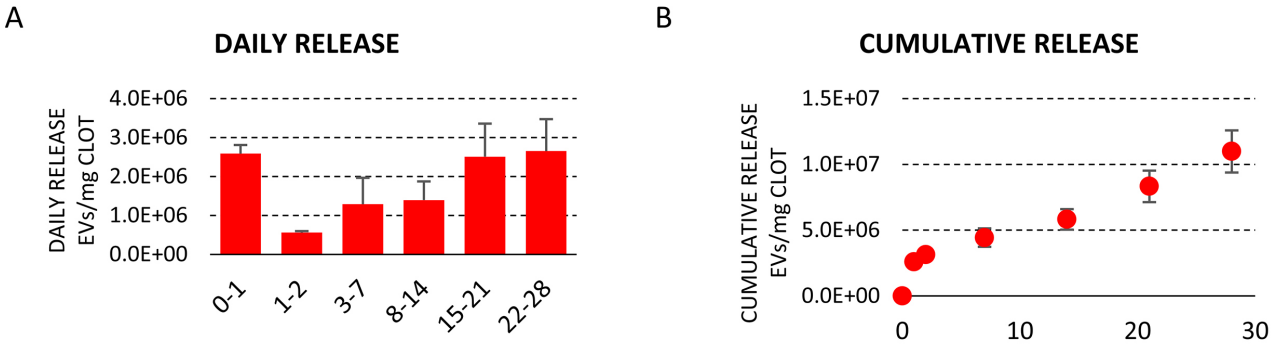

Fig. 2. Release of EVs after incorporation into PRP gels. (A) Daily EV release per mg of clot (PRP gel) over a 28-day period. (B) Cumulative EV release per mg of clot (PRP gel) over a 28-day period. Data are presented as mean ± SD (n = 6).

was observed (3% ± 4 in the second week, 5% ± 5 in the third week, and 4% ± 4 in the fourth week). Overall, 20 % of the incorporated EVs were released during the 4-week analysis period.

3.4 Released EVs Interact With Chondrocytes and Are Internalized by Cartilage Explants

The regenerative and interaction properties of the EVs released from the platelet gel after 2 days were evaluated and compared against freshly purified EVs (which had not undergone gel embedding). These comparative analyses were performed using primary OA chondrocytes (positive for lineage markers CD73/CD44 and negative for leukocyte contamination, **Supplementary Fig. 1**) in both 2D monolayers and 3D microfluidic models, as well as on native OA cartilage explants. Regarding the 2D EV–chondrocyte interaction, flow cytometry analysis revealed no statistically significant differences in MFI in the FITC channel between chondrocytes treated with purified EVs and those treated with gel-released EVs (Fig. 3A). Crucially, incubation with the supernatant harvested from unloaded vehicle platelet gels did not alter the background fluorescence of the chondrocytes, ruling out any confounding autofluorescence from the gel matrix. To validate these interaction dynamics in a more biomimetic context, an equivalent dose of either purified or gel-released EVs was administered to OA chondrocytes cultured within a 3D microfluidic platform designed to mimic the native cartilage extracellular matrix (ECM) architecture (Fig. 3B). Consistent with the 2D monolayer observations, quantitative analysis of the total intracellular EV fluorescence confirmed that both vesicle formulations interacted similarly with the cells. Indeed,

no significant differences in MFI were observed between the two experimental conditions (arbitrary MFI of chondrocytes with purified EVs vs. chondrocytes with EVs released from loaded platelet gel: 17 ± 1 vs. 17 ± 3, respectively; n = 3, p = 0.96). These results demonstrate that the embedding and subsequent release process does not impair the functional capability of EVs to interact with target cells in 3D, while also suggesting their capacity to actively migrate through the surrounding matrix. Finally, to confirm this tissue-penetrating potential under more physiological conditions, multimodal microscopy was performed on OA cartilage explants. Following 48 hours of direct contact with the EV-loaded platelet gels, a robust and positive EV-associated signal was clearly detectable within the deep layers of the cartilage tissue, penetrating up to a depth exceeding 200 µm (Fig. 3C).

3.5 Effect of PRP and EVs on Chondrocytes From OA Patients

The effect of either purified EVs alone or the secretome released from PRP clots, either unloaded or loaded with EVs (PRP-EVs), was evaluated on 3D chondrocyte pellets from OA patients, with a specific focus on the extracellular matrix. After 2 weeks of treatment, gene expression analysis revealed that PRP-EVs induced a significant downregulation of all evaluated matrix metalloproteinases involved in cartilage degradation (*MMP1*, *MMP3* and *MMP13*) (Fig. 4A). Notably, *MMP13* expression was also downregulated by PRP alone (Fig. 4A). A similar direction toward a stronger reduction by PRP-EVs was observed for *CCL5*, which encodes an inflammatory chemokine that drives the release of catabolic enzymes, including MMPs (Fig. 4A). Given these effects on matrix remodeling genes, the cumulative activity of released MMPs was evaluated at the end of the 2-week treatment period (Fig. 4B). Consistently, a significant reduction in enzymatic activity was observed exclusively in the PRP-EVs group. Furthermore, cumulative levels of released nitric oxide (NO), a key driver of cartilage degradation that inhibits ECM synthesis and activates matrix-degrading enzymes, were monitored over the 2-week period (Fig. 4C). PRP-EVs treatment significantly reduced NO production compared to all other experimental conditions, while PRP alone reduced NO release relative to the untreated pathological cells. Taken together, these data clearly demonstrated the profound impact of PRP-EVs on OA chondrocytes, as this treatment profile clustered furthest from the pathological control cells, followed by PRP alone, and lastly by pure EVs, which exerted the weakest effect (Fig. 4D). Notably, the cumulative MMP activity mirrored the expression profiles of *MMP1* and *MMP3*, with these three parameters grouping under the same second-level node. Hierarchical clustering also showed a close relationship between *CCL5* expression and NO production, observed in other cell types, which coupled under the same primary node. Finally, because fibrosis is a key phenotypic hallmark associated with cartilage damage and OA progression, the protein levels of Collagen types I, II and X were evaluated. PRP-EV treatment significantly increased the levels of "healthy" Collagen type II (Fig. 4E, **Supplementary Fig. 2**), leading to a significant elevation of the Collagen II to Collagen I ratio (Fig. 4E). Additionally, EVs showed a reduction in Collagen X expression, although this effect did not reach statistical significance compared to untreated control cells (p = 0.14). Also, when compared to the PRP-alone group, PRP-EVs combined treatment displayed a downward trend ($p \leq 0.10$), whereas PRP alone slightly increased Collagen X levels relative to pathological controls (Fig. 4F, **Supplementary Fig. 2**).

3.6 Effect of PRP and EVs on Synoviocytes From OA Patients

The effect of either purified EVs alone or the secretome released from PRP clots, either unloaded or loaded with EVs (PRP-EVs), was evaluated on synoviocytes from OA patients (positive for lineage marker CD73 and negative for monocyte and leukocyte markers, **Supplementary Fig. 1**). The evaluated genes encompassed several functional categories: inflammation and chemotaxis (*CCL2*, *CCL5*, *CXCL8*, *CXCL9*, *CXCL10* and *IL6*), extracellular matrix homeostasis and cell adhesion (*CD44*, *HAS1*, *HAS2*, *HAS3* and *ICAM1*), immunomodulation and resolution (*IL10*, *TGFB* and *IDO*), and pain signaling and inflammatory mediation (*COX2* and *NGF*). Principal component analysis (PCA) demonstrated a distinct separation from the pathological control cells for all treatment groups. Among these, pure EVs exerted the weakest effect, whereas PRP-EVs proved to be the most effective, a behavior further confirmed by heatmap analysis with hierarchical clustering (Fig. 5A). Out of all evaluated genes, six displayed statistically significant reduction, namely *CCL2*, *CXCL8*, *CXCL10*, *IL6*, *COX2* and *NGF* (Fig. 5B). Notably, PRP-EVs treatment was the most effective in modulating the expression of all six genes, while the other conditions often showed downregulation albeit no statistical difference was reached.

4. Discussion

OA is a complex, whole-joint pathological condition characterized not only by progressive cartilage degradation but also by chronic synovial inflammation and a dysfunctional intra-articular cross-talk. Current therapeutic strategies often fail to provide a simultaneous anti-inflammatory and regenerative stimulus, highlighting the need for advanced biomimetic platforms. In this work, the previous protocol developed by our group for the incorporation of MSC-derived EVs into platelet-derived fibrin gel was confirmed as feasible and reproducible. The release of the PRP-EVs combination was found to be able to promote chondrocyte homeostasis and reduce synoviocyte inflammation,

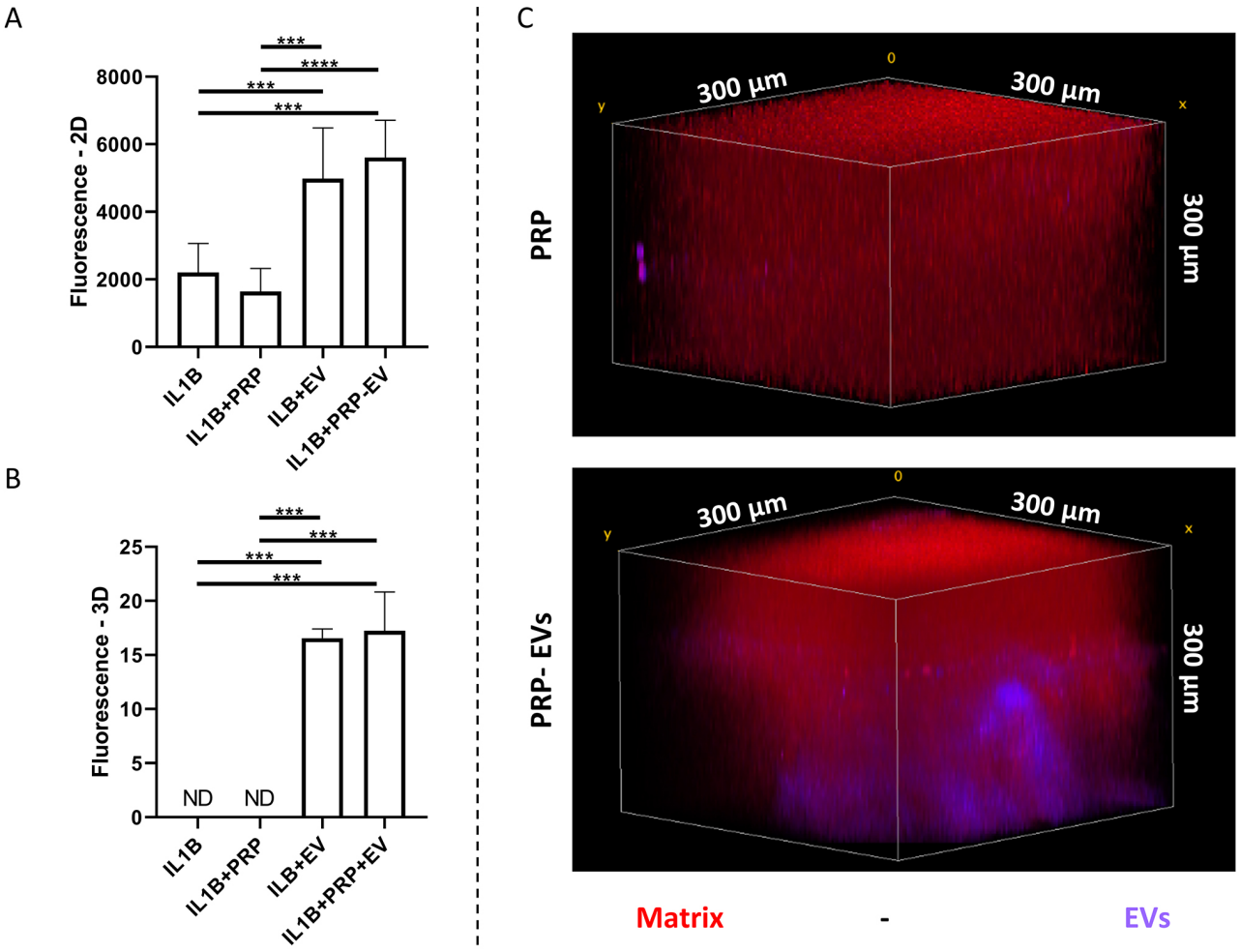

Fig. 3. Internalization of EVs into chondrocytes from OA patients. (A) Flow cytometry analysis of primary OA chondrocytes maintained in an inflammatory, osteoarthritic phenotype using interleukin-1 beta (IL-1β) and treated with purified EVs (EV), PRP gel release (PRP), or the release fraction from EV-loaded PRP gels (PRP-EV). The graph displays the geometric mean fluorescence intensity (GeoMean) in the fluorescein isothiocyanate (FITC) channel, reflecting the intracellular fluorescent EV signal across the four conditions. No statistically significant difference ($p > 0.05$) was detected between the purified EV and PRP-EV groups. Data are presented as mean ± SD (n = 3; *** $p \leq 0.001$, **** $p \leq 0.0001$ by one-way Analysis of Variance (ANOVA) followed by Tukey's post-hoc test). (B) EV internalization within the three-dimensional (3D) microfluidic model. Fluorescent signal intensity in primary OA chondrocytes cultured inside 3D microfluidic devices and incubated for 48 hours with equivalent doses of either purified EVs or EVs released from the platelet gel. The graph illustrates the mean fluorescence intensity across three independent donors. For the inflamed control (IL-1β) and the gel-release control (IL-1β + PRP), values are not displayed as they were utilized as background thresholds for differential analysis. Data are expressed as mean ± SD (n = 3; *** $p \leq 0.001$ by one-way ANOVA followed by Tukey's post-hoc test). (C) 3D cartilage tissue penetration. Representative 3D reconstructions of OA cartilage explants after a 48-hour incubation with either unloaded (vehicle) or EV-loaded platelet gels. The Coherent Anti-Stokes Raman Scattering (CARS) signal (red) identifies the dense cartilage extracellular matrix (ECM), whereas the two-photon excited fluorescence (TPEF) signal (blue) indicates the distribution of fluorescently labeled EVs. Bounding box dimensions in µm are indicated relative to the origin vertex.

potentially contributing to overall joint balance. These results pave the way for future use of PRP-EVs gels for cartilage defects by acting as a multi-target disease-modifying therapy.

A primary objective of this study was to validate the technical robustness and standardizability of our protocol for incorporating ASC-EVs into a platelet-derived fibrin gel (PRP), directly expanding upon the framework established in our previous work [22]. The experimental findings demonstrated a high degree of technical continuity, confirming that embedment efficiency, particle loading density and longitudinal elution dynamics over a 4-week window closely aligned with our baseline models. This structural reliability proves the method is highly reproducible despite the inherent biological variability of different donors. Crucially, the process of $CaCl_2$ activation and subsequent

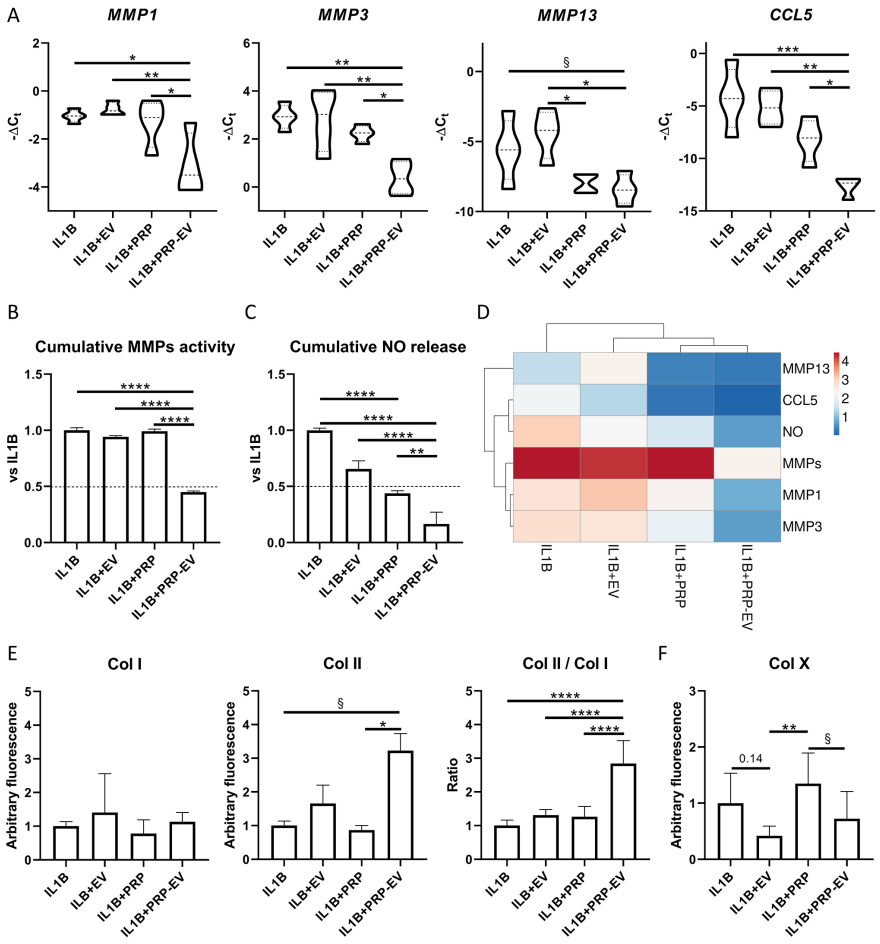

Fig. 4. Effect of pure EVs or the release of PRP gels without (PRP) or with EVs (PRP-EVs) on OA chondrocytes. (A) Upregulation or downregulation of *MMP1/3/13* and *CCL5* in OA patients' chondrocyte pellets under IL-1β treatment, to sustain pathologic phenotype, exposed to EVs, release of PRP gels (PRP) or release of combined PRP gel + EVs (PRP-EVs) for 14 days. Data are reported as –ΔCt with respect to *RPLP0* Ct values for each gene. Mean ± SD, n ≥ 3. § $p \leq 0.1$; * $p \leq 0.05$; ** $p \leq 0.01$; *** $p \leq 0.001$. Statistical significance was evaluated using One-Way ANOVA with a Tukey post-hoc test. (B) Cumulative MMP activity in the supernatant of OA patients' chondrocyte pellets under IL-1β treatment, to sustain pathologic phenotype, exposed to EVs, release of PRP gels (PRP) or release of combined PRP gel + EVs (PRP-EVs) for 14 days. Data are reported as relative activity with respect to the IL-1β condition set as 1. Mean ± SD, n ≥ 3. **** $p \leq 0.0001$. Statistical significance was evaluated using One-Way ANOVA with a Tukey post-hoc test. (C) Cumulative NO release in the supernatant of OA patients' chondrocyte pellets under IL-1β treatment, to sustain pathologic phenotype, exposed to EVs, release of PRP gels (PRP) or release of combined PRP gel + EVs (PRP-EVs) for 14 days. Data are reported as relative NO release with respect to IL-1β condition set as 1. Mean ± SD, n ≥ 3. ** $p \leq 0.01$; **** $p \leq 0.0001$. Statistical significance was evaluated using One-Way ANOVA with a Tukey post-hoc test. (D) Heat Map and hierarchical clustering of gene expression, MMP activity (MMPs) and NO release values. Gene expression abundance ratios were calculated from –ΔCt data ($2^{-\Delta Ct}$) and the IL-1β condition was set as 1. Input values were ln(x+1)-transformed. Unit variance scaling was applied to rows. Both rows and columns were clustered using correlation distance and average linkage. Red shades for higher abundance/activity values, blue shades for reduced ones. (E) Arbitrary levels of Collagen I and Collagen II, and Coll II *vs* Col I ratio, in OA patients' chondrocyte pellets under IL-1β treatment, to sustain pathologic phenotype, exposed to EVs, release of PRP gels (PRP) or release of combined PRP gel + EVs (PRP-EVs) for 14 days. Data are reported as relative protein amount with respect to the IL-1β condition set as 1. Mean ± SD, n ≥ 5. § $p \leq 0.1$, * $p \leq 0.05$, **** $p \leq 0.0001$. Statistical significance was performed using Kruskal-Wallis with a Dunn post-hoc test for single Col I and Col II evaluations. For Col II *vs* Col I ratio evaluation, statistical significance was performed using One-Way ANOVA with a Tukey post-hoc test. (F) Arbitrary levels of Collagen X in OA patients' chondrocyte pellets under IL-1β treatment, to sustain pathologic phenotype, exposed to EVs, release of PRP gels (PRP) or release of combined PRP gel + EVs (PRP-EVs) for 14 days. Data are reported as relative protein amount with respect to the IL-1β condition set as 1. Mean ± SD, n ≥ 5. § $p \leq 0.1$, ** $p \leq 0.01$. Statistical significance was evaluated using One-Way ANOVA with a Tukey post-hoc test.

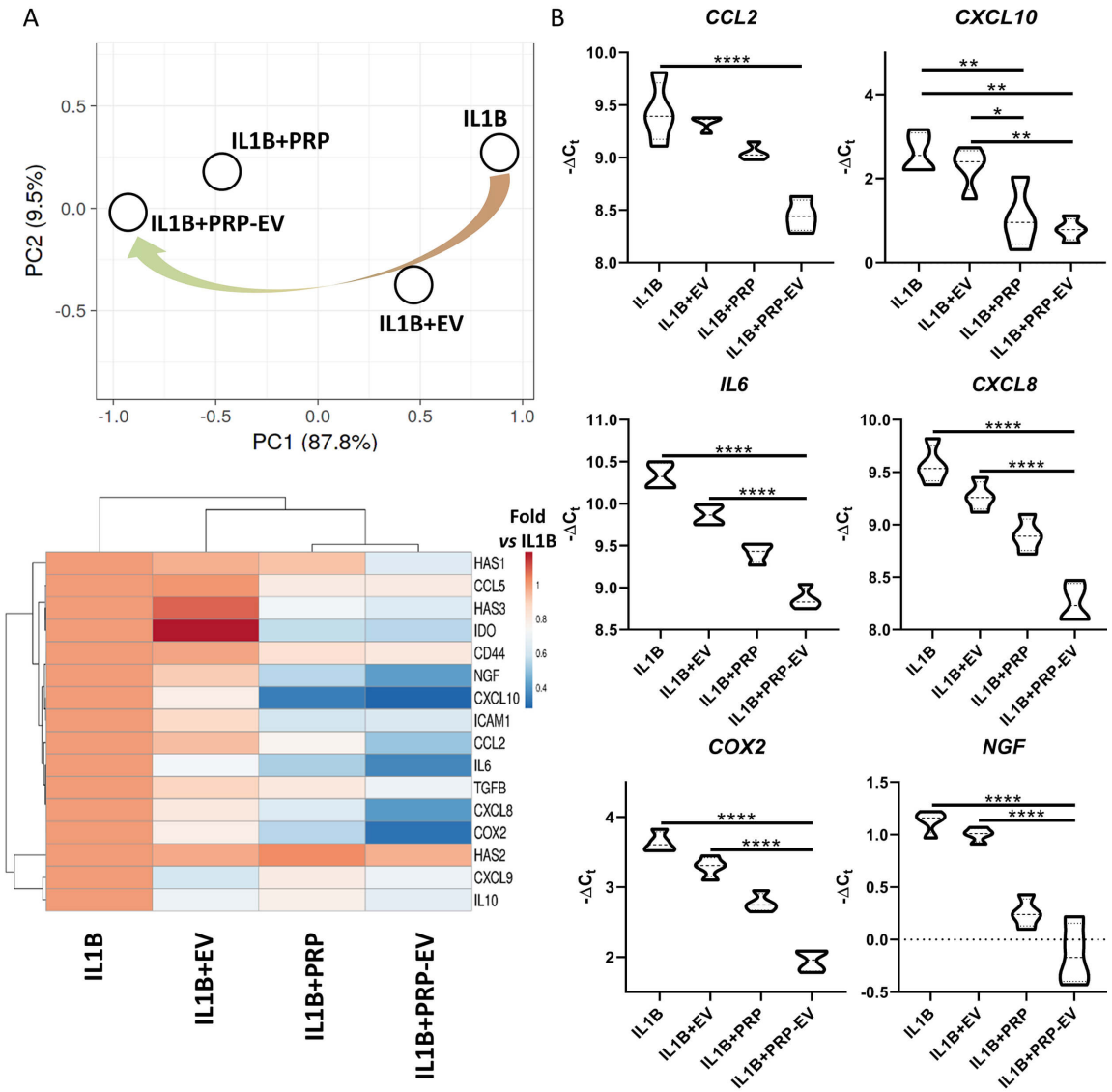

Fig. 5. Effect of pure EVs or the release of PRP gels without (PRP) or with EVs (PRP-EVs) on OA synoviocytes. (A) Overall effect of EVs, release of PRP gels (PRP) or release of combined PRP gel + EVs (PRP-EVs) for 2 days on OA patients' synoviocytes under IL-1β treatment, to sustain pathologic phenotype. Gene expression abundance ratios were calculated from –ΔCt data ($2^{-\Delta Ct}$) and the IL-1β condition was set as 1. For PCA, no scaling was applied to rows; SVD with imputation was used to calculate principal components. The X- and Y-axes show principal component 1 and principal component 2, which explain 87.8% and 9.5% of the total variance, respectively. For the heatmap with hierarchical clustering, no scaling was applied to rows. Both rows and columns were clustered using correlation distance and average linkage. (B) Upregulation or downregulation of *CCL2*, *CXCL8*, *CXCL10*, *IL6*, *COX2* and *NGF* in OA patients' synoviocytes under IL-1β treatment, to sustain pathologic phenotype, exposed to EVs, release of PRP gels (PRP) or release of combined PRP gel + EVs (PRP-EVs) for 2 days. Only genes with at least one statistically significant difference between any condition (fold ≥2 or ≤0.5 and *p*-value ≤ 0.05) are shown. Data are reported as –ΔCt with respect to *TBP* Ct values for each gene. Mean ± SD, n ≥ 4. * $p \leq 0.05$; ** $p \leq 0.01$; **** $p \leq 0.0001$. Statistical significance was evaluated using One-Way ANOVA with a Tukey post-hoc test.

matrix entrapment did not compromise the functional integrity of the biologics. In both two-dimensional and three-dimensional microfluidic models, the MFI increase in OA chondrocytes interacting with gel-released EVs was statistically identical to that of those treated with directly purified EVs, replicating previous data [22]. This result confirms that the scaffolding environment preserves crucial EV surface receptors and cellular uptake mechanisms. Finally, multimodal microscopy of human OA cartilage explants showed that the released particles successfully achieved deep matrix penetration into degenerated tissue zones, establishing this framework as a stable and robust delivery system.

Together with the ability to be incorporated, released and transferred, the therapeutic efficacy of ASC-EVs is heavily dictated by their bioactive miRNA cargo. Our quantitative molecular profiling revealed that 20 highly abundant miRNAs accounted for 81% of the total genetic message, showing a profound quantitative asymmetry favoring tissue preservation over degradation. Within the cartilage homeostasis category, protective miRNAs (predominantly miR-24-3p [29,30,31], miR-222-3p [32,33] and miR-193b-3p [34,35]) outweighed destructive ones by nearly fourfold (27 % vs 7 %), aligning with established roles for these sequences in preserving the chondrocyte phenotype and resisting matrix breakdown. Mechanistically, miR-24-3p has been shown to repress A Disintegrin and Metalloproteinase with Thrombospondin Motifs-5 (ADAMTS-5) and caspase-3 [30], thereby directly blunting aggrecanase activity and chondrocyte apoptosis, while miR-222-3p maintains the differentiated state by targeting histone deacetylase-4 (HDAC4) [33], a known suppressor of Runx2 and cartilage hypertrophy. Furthermore, miR-193b-3p directly regulates HDAC3 [34], promoting a chromatin state accessible for SRY-Box Transcription Factor 9 (SOX9)-driven collagen type II transcription. This signature provides a robust mechanistic explanation for the potent anti-catabolic and anti-inflammatory activity exerted on the joint microenvironment, and mirrors the results presented in the pilot study with an almost superimposable array of pro-chondrogenic factors in ASC-EVs from a different set of donors. Regarding miRNAs' role in osteoarthritis synoviocytes homeostasis, data are still poor, although recent *in vivo* data showed how EVs from fat pad MSCs reduced proliferation, inflammation-related molecular profiles and secretion of pro-inflammatory molecules in pathologic synoviocytes [36], and that this shared potential relies on the shuttled cargo similarly acting on both cell types.

When evaluated in a 3D chondrocyte pellet model, the combined PRP-EV formulation demonstrated clear superiority over individual treatments, with hierarchical clustering placing the PRP-EV profile furthest from pathological control cells. This superior performance is driven by several concurrent mechanisms: PRP-EVs induced a profound downregulation of primary degradative collagenases (*MMP1*, *MMP3* and *MMP13*), which was functionally mirrored by a significant reduction in cumulative enzymatic MMP activity. MMP increases are among the key mediators involved in cartilage structure degradation in OA pathology [37], alongside oxidative damage due to NO release in response to inflammation. NO is part of the catabolic functional program in chondrocytes which are the major intra-articular contributors [38]. Of note, PRP-EVs blunted in a similar way the production of NO and the expression of the chemokine *CCL5*, reported in other cell types to be directly linked with NO release [39]. The concurrent inhibition of *CCL5* and NO points toward an interruption of the nuclear factor kappaB (NF-κB) signaling cascade, a master regulator of OA catabolism [40] that is standardly fueled by PRP-derived pro-inflammatory cytokines but here post-transcriptionally quenched by the EV cargo. Strikingly, while PRP alone is effective in promoting cartilage repair albeit often promoting fibrous tissue formation [20,21], the addition of ASC-EVs shifted the balance toward native hyaline regeneration, significantly elevating the critical Collagen II to Collagen I ratio. Both pure EVs and PRP-EVs successfully suppressed Collagen X expression, a marker of chondrocyte hypertrophy [41], counteracting the hypertrophic induction seen with PRP alone and proving that the EVs, directing PRP away from fibrosis and toward high-quality matrix synthesis, act as a phenotypic brake as reported in animal models [42]. This phenotypic steering is likely dependent on the capability of EV-miRNAs to modulate transforming growth factor-β (TGF-β)/bone morphogenic protein (BMP) signalling pathways [43], effectively balancing the pro-fibrotic signalling molecules natively present in platelet concentrates.

Eventually, because OA is a whole-joint disease where synovial inflammation cross-talks with cartilage degradation, a successful disease-modifying therapy must address the pathologic synovium. In human OA synoviocytes, as observed in the chondrocyte model, the PRP-EVs combination exerted the most robust therapeutic impact, significantly downregulating a panel of six pivotal pathological genes: *CCL2*, *CXCL8*, *CXCL10* and *IL6* (governing inflammation and chemotaxis), alongside *COX2* and *NGF* (governing prostaglandin synthesis, joint pain signaling and hyperalgesia). If the role of synovitis inflammation [2] and its therapeutic management is largely described in OA [44], pain and its dependence on synovium is less described. Notably, pivotal EVs treatment *in vivo* demonstrated pain reduction [45,46], suggesting that EVs may alleviate joint algesia by decreasing *NGF* and *COX2* expression, which are notorious local triggers for sensory nerve sensitization within the subchondral bone and synovium [47,48]. This dual action, silencing chemotactic recruitment via C-C motif chemokine ligand-2 (CCL-2)/C-X-C motif chemokine ligands (CXCLs) and resolving nociceptive signalling, enhances their comprehensive therapeutic efficacy across the entire joint ecosystem and potentially improves overall patient outcomes.

Overall, all three formulations evaluated demonstrated efficacy in counteracting *in vitro* chondrocyte and synoviocyte inflammation. However, pure EVs and the secretome from unloaded PRP gels alone exhibited less pronounced downregulatory effects, frequently failing to achieve statistical significance across all evaluated targets. Notably, the PRP gel secretome outperformed pure EVs across the majority of tested parameters, providing a mechanistic justification for its widespread use in current clinical practice. Nevertheless, a major drawback of PRP therapy remains its tendency to drive phenotypic shifts toward lower-quality fibrous tissue, a phenomenon also observed

in our 3D chondrocyte model. Conversely, while pure EVs exerted a less potent immediate effect than the PRP secretome, they demonstrated an intrinsic capacity to direct more biomimetic, hyaline-like cartilage regeneration. This distinction suggests that rather than serving as a standalone primary driver of tissue repair, EVs may function more effectively as an instructive adjuvant. From this perspective, the superior efficacy of the combined PRP-EV product confirms that the bioactive factors released by the platelet gel work synergistically with EVs, effectively disrupting the positive feedback loop of synovial inflammation and joint pain through a more physiologically balanced mechanism.

Limitations

This study has limitations that should be acknowledged. First, the evaluation relied on *in vitro* models, which inherently only partially recapitulate the complex, multitissue physiology of the native joint. To mitigate this limitation and closely mimic the degenerated environment, primary cells harvested directly from OA patients were utilized and maintained under chronic inflammatory conditions. Nevertheless, we acknowledge that the present *in vitro* setup does not allow for the evaluation of the systemic immune response, clearance kinetics or joint-related functional outcomes, meaning these findings must be interpreted within a strictly preclinical framework. Additionally, a formal analysis of EV stability and release kinetics over a 4-week gel incubation period was not performed. In our setting, the isolation and characterization of gel-released ASC-EVs (e.g., sorting to separate them from PRP-EVs) would require high-sensitivity instrumentation and large volumes of input materials that were unavailable. Nevertheless, monitoring and maintaining EV stability and therapeutic effects over extended periods remains a key challenge. To address these aspects, an *in vivo* study is currently ongoing to rigorously validate the regenerative and protective efficacy of the PRP-EV formulation in a living cartilage defect model where both the long-term outcomes and functional effects, mirroring the maintenance of EVs efficacy over time, will be evaluated. Second, this work focused primarily on the joint's stromal elements, specifically evaluating chondrocytes and synoviocytes. Future investigations will expand upon these findings by testing the effects of pure EVs, PRP and the combined PRP-EV secretome on the joint's immune compartment, with a specific emphasis on macrophage polarization and activation. Finally, because our primary focus was on evaluating the cumulative biological message conveyed by the whole EV-miRNA cargo, specific knockdown or overexpression experiments of individual candidate miRNAs were not performed. To address this and uncover the exact molecular mechanisms driving the observed phenotypic shifts, a comprehensive high-throughput characterization of the EV cargo, using advanced fingerprinting techniques such as Next-Generation Sequencing (NGS), will be required in future studies. This molecular-level resolution will also be highly valuable in dissecting potential donor-to-donor variability in therapeutic efficacy. In the present study, due to the limited number of donors, such variability was not explicitly analysed. Instead, priority was given to maximizing cohort diversity by including both sexes and a broad age range to capture a wider biological spectrum.

5. Conclusions

Our findings demonstrate that integrating ASC-EVs into a PRP fibrin matrix establishes a paradigm shift in whole-joint bio-orchestration, moving beyond simple drug delivery to actively reprogram the pathological cross-talk between degenerating cartilage and an inflamed synovium. By balancing the potent stimuli of platelet growth factors with the homeostatic, anti-fibrotic "braking" action of EV-shuttled miRNAs, this platform provides a blueprint for multi-component, biomaterial-stabilized biologics capable of dynamically reshaping diseased microenvironments over extended periods. Given its clinically scalable and potentially autologous nature, this dual-action framework lays an adaptable foundation for point-of-care regenerative medicine, offering a therapeutic concept that could be extended beyond osteoarthritis to other complex, inflammation-driven musculoskeletal disorders.

Availability of Data and Materials

The datasets utilized and analyzed in the current study are available from the corresponding author upon reasonable request. The raw data are deposited to OSF and will be publicly available as of the date of publication at: https://osf.io/sc7p6/overview?view_only=a969f21fb9894bf9a07e655ee4b28896.

Author Contributions

ER and GP designed the research study. ER and MT developed the methodology. AMN was in charge of the software used in the study. PDL validated the results. ER and MT performed the formal analysis. ER and MT conducted the investigation. FV, SL and LL obtained the resources and curated the data visualization. PDL helped in data curation. ER prepared the original draft. LdG review and edited the manuscript and performed the formal analysis. AMN curated the data visualization. GP supervised the project and performed the formal analysis. LdG was in charge of project administration. GP acquired the funding. All authors contributed to editorial changes in the manuscript. All authors read and approved the final manuscript. All authors have participated sufficiently in the work and agreed to be accountable for all aspects of the work.

Ethics Approval and Consent to Participate

The study was conducted in accordance with the Declaration of Helsinki. The research protocol was approved by Comitato Etico Territoriale Lombardia 1 ("Gel di fibrina caricato con vescicole extracellulari per il trattamento delle lesioni cartilaginee delle articolazioni", approval on date 22/05/2024, registered under number CET 186-2024), and all of the participants provided signed informed consent.

Acknowledgment

We gratefully acknowledge the personnel of Laboratorio di Biotecnologie Applicate all'Ortopedia for support.

Funding

This research was funded by the European Union—Next Generation EU—NRRP M6C2—Investment 2.1 Enhancement and strengthening of biomedical research in the NHS—Project Code PNRR-MCNT2-2023-12377836 (CUP Master C43C24000460001). The APC was funded by the European Union—Next Generation EU—NRRP M6C2—Investment 2.1 Enhancement and strengthening of biomedical research in the NHS—Project Code PNRR-MCNT2-2023-12377836 (CUP Master C43C24000460001).

Conflicts of Interest

The authors declare no conflicts of interest. Enrico Ragni is serving as one of the Guest editors of this journal. We declare that Enrico Ragni had no involvement in the peer review of this article and has no access to information regarding its peer review. Full responsibility for the editorial process for this article was delegated to Nikos Karamanos.

Declaration of AI and AI-Assisted Technologies in the Writing Process

During the preparation of this work, the authors used Gemini 1.5 Pro in order to check spelling and grammar, and Gemini 3.5 Flash to create the graphical abstract. After using this tool, the authors reviewed and edited the content as needed and take full responsibility for the content of the publication.

Supplementary Material

Supplementary material associated with this article can be found in the online version, at https://doi.org/10.31083/FBL54998.

References

[1] Oliveira S, Hinckel BB, Silva FS, Carvalho Ó, Leal A. A guide to articular cartilage functioning: a comprehensive review, current challenges and mechanobiological solutions. Progress in Biomedical Engineering (Bristol, England). 2025; 7: 10.1088/2516–1091/ade83a. https://doi.org/10.1088/2516-1091/ade83a

[2] Sanchez-Lopez E, Coras R, Torres A, Lane NE, Guma M. Synovial inflammation in osteoarthritis progression. Nature Reviews. Rheumatology. 2022; 18: 258–275. https://doi.org/10.1038/s41584-022-00749-9

[3] Delattre BMA, Hilbert T, Kutaish H, Crowe LA, Poletti PA, Menetrey J, et al. Healthy knee cartilage T2 mapping assessed with GRAPPATINI and multi-echo spin-echo (MESE) at 3T: regional values, longitudinal repeatability and method agreement. Quantitative Imaging in Medicine and Surgery. 2026; 16: 337. https://doi.org/10.21037/qims-2025-1-2462

[4] GBD 2021 Osteoarthritis Collaborators. Global, regional, and national burden of osteoarthritis, 1990-2020 and projections to 2050: a systematic analysis for the Global Burden of Disease Study 2021. The Lancet. Rheumatology. 2023; 5: e508–e522. https://doi.org/10.1016/S2665-9913(23)00163-7

[5] García JR, Acuña AJ, Villareal JB, Saad Berreta R, Gonzalez Ayala S, del Baño-Barragán L, et al. New horizons in cartilage repair: update on treatment trends and outcomes. Journal of Cartilage & Joint Preservation. 2024; 2: 100179. https://doi.org/10.1016/j.jcjp.2024.100179

[6] Caplan AI. Mesenchymal Stem Cells: Time to Change the Name! Stem Cells Translational Medicine. 2017; 6: 1445–1451. https://doi.org/10.1002/sctm.17-0051

[7] Wei W, Ao Q, Wang X, Cao Y, Liu Y, Zheng SG, et al. Mesenchymal Stem Cell-Derived Exosomes: A Promising Biological Tool in Nanomedicine. Frontiers in Pharmacology. 2021; 11: 590470. https://doi.org/10.3389/fphar.2020.590470

[8] Torres-Torrillas M, Rubio M, Damia E, Cuervo B, Del Romero A, Peláez P, et al. Adipose-Derived Mesenchymal Stem Cells: A Promising Tool in the Treatment of Musculoskeletal Diseases. International Journal of Molecular Sciences. 2019; 20: 3105. https://doi.org/10.3390/ijms20123105

[9] Ragni E, Perucca Orfei C, Sinigaglia F, de Girolamo L. Joint Tissue Protective and Immune-Modulating miRNA Landscape of Mesenchymal Stromal Cell-Derived Extracellular Vesicles under Different Osteoarthritis-Mimicking Conditions. Pharmaceutics. 2022; 14: 1400. https://doi.org/10.3390/pharmaceutics14071400

[10] Ragni E, Colombini A, Viganò M, Libonati F, Perucca Orfei C, Zagra L, et al. Cartilage Protective and Immunomodulatory Features of Osteoarthritis Synovial Fluid-Treated Adipose-Derived Mesenchymal Stem Cells Secreted Factors and Extracellular Vesicles-Embedded miRNAs. Cells. 2021; 10: 1072. https://doi.org/10.3390/cells10051072

[11] Ragni E, Perucca Orfei C, De Luca P, Mondadori C, Viganò M, Colombini A, et al. Inflammatory priming enhances mesenchymal stromal cell secretome potential as a clinical product for regenerative medicine approaches through secreted factors and EV-miRNAs: the example of joint disease. Stem Cell Research & Therapy. 2020; 11: 165. https://doi.org/10.1186/s13287-020-01677-9

[12] Kang J, Jie L, Fu H, Zhang L, Lu G, Yu L, et al. Adipose Mesenchymal Stem Cells Derived Exosomes Ameliorates KOA Cartilage Damage and Inflammation by Activation of PINK1-Mediated Mitochondrial Autophagy. FASEB Journal : Official Publication of the Federation of American Societies for Experimental Biology. 2025; 39: e70811. https://doi.org/10.1096/fj.202501185R

[13] Chen KT, Huang CC, Yadav VK, Pikatan NW, Fong IH, Kuo KT, et al. Gluteal adipose-derived stem cell exosomes promote macrophage polarization and cartilage regeneration in osteoarthritis via PTPRC modulation. Biomedicine & Pharmacotherapy = Biomedecine & Pharmacotherapie. 2026; 196: 119130. https://doi.org/10.1016/j.biopha.2026.119130

[14] Akbar A, Dilogo IH, Antarianto RD, Kousar I, Tantry AJ, Canintika AF. Intra-Articular Injection of Adipose-Derived-MSC Exosomes and Hyaluronic Acid in Sheep Knee Osteoarthritic Models Enhances Hyaline Cartilage Regeneration. Biomedicines. 2025; 13: 3070. https://doi.org/10.3390/biomedicines13123070

[15] Woo CH, Kim HK, Jung GY, Jung YJ, Lee KS, Yun YE, et al. Small extracellular vesicles from human adipose-derived stem cells attenuate cartilage degeneration. Journal of Extracellular Vesicles. 2020; 9: 1735249. https://doi.org/10.1080/20013078.2020.1735249

[16] Fu YJ, Jian J, Liu C, Yi YF, Ding YT, Wen J, et al. Application of stem cell-derived exosomes in bone and joint diseases: Recent advances enabled by diverse carrier technologies. World Journal of Stem Cells. 2025; 17: 113631. https://doi.org/10.4252/wjsc.v17.i11.113631

[17] Rahmati S, Khazaei M, Nadi A, Alizadeh M, Rezakhani L. Exosome-loaded scaffolds for regenerative medicine in hard tissues. Tissue & Cell. 2023; 82: 102102. https://doi.org/10.1016/j.tice.2023.102102

[18] Su CY, Kuo YP, Nieh HL, Tseng YH, Burnouf T. Quantitative assessment of the kinetics of growth factors release from platelet gel. Transfusion. 2008; 48: 2414–2420. https://doi.org/10.1111/j.1537-2995.2008.01862.x

[19] Jalowiec JM, D'Este M, Bara JJ, Denom J, Menzel U, Alini M, et al. An In Vitro Investigation of Platelet-Rich Plasma-Gel as a Cell and Growth Factor Delivery Vehicle for Tissue Engineering. Tissue Engineering. Part C, Methods. 2016; 22: 49–58. https://doi.org/10.1089/ten.TEC.2015.0223

[20] Carneiro MDO, Barbieri CH, Barbieri Neto J. Platelet-rich plasma gel promotes regeneration of articular cartilage in knees of sheeps. Acta Ortopedica Brasileira. 2013; 21: 80–86. https://doi.org/10.1590/S1413-78522013000200003

[21] Papalia R, Diaz Balzani L, Torre G, Tirindelli MC, Nobile C, Maffulli N, et al. Intraoperative application Platelet rich fibrin, postoperative injections OF PRP or microfracture only for osteochondral lesions of the knee: a five-year retrospective evaluation. Journal of Biological Regulators and Homeostatic Agents. 2016; 30: 41–49.

[22] Ragni E, De Luca P, Landoni S, Valli F, Mortati L, Palombella S, et al. High efficiency protocol for platelet derived fibrin gel loaded with mesenchymal stromal cells extracellular vesicles. Regenerative Therapy. 2024; 26: 442–457. https://doi.org/10.1016/j.reth.2024.06.020

[23] Taiana MM, Landoni S, Valli F, de Girolamo L, Ragni E, de Luca P. Extracellular vesicles outperform adipose derived-mesenchymal stromal cells in alleviating osteoarthritis chondrocyte inflammation in vitro when incorpo-rated into platelet-derived fibrin gel. Ligaments and Tendons Journal. 2026; 16. https://doi.org/10.32098/mltj_2026_6387

[24] Chang L, Xia J. MicroRNA Regulatory Network Analysis Using miRNet 2.0. Methods in Molecular Biology (Clifton, N.J.). 2023; 2594: 185–204. https://doi.org/10.1007/978-1-0716-2815-7_14

[25] Metsalu T, Vilo J. ClustVis: a web tool for visualizing clustering of multivariate data using Principal Component Analysis and heatmap. Nucleic Acids Research. 2015; 43: W566–70. https://doi.org/10.1093/nar/gkv468

[26] Toh WS, Lai RC, Zhang B, Lim SK. MSC exosome works through a protein-based mechanism of action. Biochemical Society Transactions. 2018; 46: 843–853. https://doi.org/10.1042/BST20180079

[27] Chevillet JR, Kang Q, Ruf IK, Briggs HA, Vojtech LN, Hughes SM, et al. Quantitative and stoichiometric analysis of the microRNA content of exosomes. Proceedings of the National Academy of Sciences of the United States of America. 2014; 111: 14888–14893. https://doi.org/10.1073/pnas.1408301111

[28] Endisha H, Rockel J, Jurisica I, Kapoor M. The complex landscape of microRNAs in articular cartilage: biology, pathology, and therapeutic targets. JCI Insight. 2018; 3: e121630. https://doi.org/10.1172/jci.insight.121630

[29] Sun Y, You Y, Wu Q, Hu R, Dai K. Senescence-targeted MicroRNA/Organoid composite hydrogel repair cartilage defect and prevention joint degeneration via improved chondrocyte homeostasis. Bioactive Materials. 2024; 39: 427–442. https://doi.org/10.1016/j.bioactmat.2024.05.036

[30] Xu J, Qian X, Ding R. MiR-24-3p attenuates IL-1β-induced chondrocyte injury associated with osteoarthritis by targeting BCL2L12. Journal of Orthopaedic Surgery and Research. 2021; 16: 371. https://doi.org/10.1186/s13018-021-02378-6

[31] Philipot D, Guérit D, Platano D, Chuchana P, Olivotto E, Espinoza F, et al. p16INK4a and its regulator miR-24 link senescence and chondrocyte terminal differentiation-associated matrix remodeling in osteoarthritis. Arthritis Research & Therapy. 2014; 16: R58. https://doi.org/10.1186/ar4494

[32] Liu X, Feng F, Jin Y, Ma C, Zhu Q, You Y, et al. Loss of the miR-221/222 Cluster Promotes the Pathogenesis of Osteoarthritis in Inflamed Mouse Chondrocytes and Osteoarthritis Models. Inflammation. 2025; 49: 2. https://doi.org/10.1007/s10753-025-02411-4

[33] Song J, Jin EH, Kim D, Kim KY, Chun CH, Jin EJ. MicroRNA-222 regulates MMP-13 via targeting HDAC-4 during osteoarthritis pathogenesis. BBA Clinical. 2014; 3: 79–89. https://doi.org/10.1016/j.bbacli.2014.11.009

[34] Meng F, Li Z, Zhang Z, Yang Z, Kang Y, Zhao X, et al. MicroRNA-193b-3p regulates chondrogenesis and chondrocyte metabolism by targeting HDAC3. Theranostics. 2018; 8: 2862–2883. https://doi.org/10.7150/thno.23547

[35] Chen X, Zhang R, Zhang Q, Xu Z, Xu F, Li D, et al. Chondrocyte sheet *in vivo* cartilage regeneration technique using miR-193b-3p to target MMP16. Aging. 2019; 11: 7070–7082. https://doi.org/10.18632/aging.102237

[36] Kouroupis D, Kaplan LD, Best TM. Human infrapatellar fat pad mesenchymal stem cells show immunomodulatory exosomal signatures. Scientific Reports. 2022; 12: 3609. https://doi.org/10.1038/s41598-022-07569-7

[37] Mukherjee A, Das B. The role of inflammatory mediators and matrix metalloproteinases (MMPs) in the progression of osteoarthritis. Biomaterials and Biosystems. 2024; 13: 100090. https://doi.org/10.1016/j.bbiosy.2024.100090

[38] Rediske JJ, Koehne CF, Zhang B, Lotz M. The inducible production of nitric oxide by articular cell types. Osteoarthritis and Cartilage. 1994; 2: 199–206. https://doi.org/10.1016/s1063-4584(05)80069-x

[39] Costa RM, Cerqueira DM, Bruder-Nascimento A, Alves JV, Awata WMC, Singh S, et al. Role of the CCL5 and Its Receptor, CCR5, in the Genesis of Aldosterone-Induced Hypertension, Vascular Dysfunction, and End-Organ Damage. Hypertension (Dallas, Tex. : 1979). 2024; 81: 776–786. https://doi.org/10.1161/HYPERTENSIONAHA.123.21888

[40] Choi MC, Jo J, Park J, Kang HK, Park Y. NF-κB Signaling Pathways in Osteoarthritic Cartilage Destruction. Cells. 2019; 8: 734. https://doi.org/10.3390/cells8070734

[41] Dreier R. Hypertrophic differentiation of chondrocytes in osteoarthritis: the developmental aspect of degenerative joint disorders. Arthritis Research & Therapy. 2010; 12: 216. https://doi.org/10.1186/ar3117

[42] To K, Romain K, Mak C, Kamaraj A, Henson F, Khan W. The Treatment of Cartilage Damage Using Human Mesenchymal Stem Cell-Derived Extracellular Vesicles: A Systematic Review of *in vivo* Studies. Frontiers in Bioengineering and Biotechnology. 2020; 8: 580. https://doi.org/10.3389/fbioe.2020.00580

[43] Thielen NGM, van der Kraan PM, van Caam APM. TGFβ/BMP

Signaling Pathway in Cartilage Homeostasis. Cells. 2019; 8: 969. https://doi.org/10.3390/cells8090969

[44] Mobasheri A, Castro-Domínguez F, Gualillo O, Kluzek S, Ruiz SP, Largo R. Targeting synovial inflammation in knee osteoarthritis: translational insights for diagnosis and therapy. Journal of Orthopaedic Translation. 2026; 56: 101012. https://doi.org/10.1016/j.jot.2025.10.004

[45] Zhang S, Teo KYW, Chuah SJ, Lai RC, Lim SK, Toh WS. MSC exosomes alleviate temporomandibular joint osteoarthritis by attenuating inflammation and restoring matrix homeostasis. Biomaterials. 2019; 200: 35–47. https://doi.org/10.1016/j.biomaterials.2019.02.006

[46] Khatab S, van Osch GJ, Kops N, Bastiaansen-Jenniskens YM, Bos PK, Verhaar JA, et al. Mesenchymal stem cell secretome reduces pain and prevents cartilage damage in a murine osteoarthritis model. European Cells & Materials. 2018; 36: 218–230. https://doi.org/10.22203/eCM.v036a16

[47] Obeidat AM, Newton MD, Li J, Hu B, Ishihara S, Lammlin L, et al. Nerve Growth Factor is Sufficient to Cause Multiple Osteoarthritis-Relevant Pathologic Features in Naïve Murine Knee Joints. Arthritis & Rheumatology (Hoboken, N.J.). 2026; 10.1002/art.70168. https://doi.org/10.1002/art.70168

[48] Crofford LJ. COX-2 in synovial tissues. Osteoarthritis and Cartilage. 1999; 7: 406–408. https://doi.org/10.1053/joca.1999.0226